Energy Storage Materials 47 (2022) 262–270

Contents lists available at ScienceDirect

Energy Storage Materials

journal homepage: www.elsevier.com/locate/ensm

A 3D interconnected metal-organic framework-derived solid-state electrolyte for dendrite-free lithium metal battery

Zhongliang Li[1], Shuxian Wang[1], Junkai Shi, Yang Liu, Siyan Zheng, Hanqin Zou, Yilin Chen, Wenxi Kuang, Kui Ding, Luyi Chen, Ya-qian Lan, Yue-peng Cai*, Qifeng Zheng*

School of Chemistry, South China Normal University, 55 West Zhongsan Rd., Guangzhou, Guangdong 510006, China

ARTICLE INFO

Keywords:
Solid-state electrolyte
Interconnected metal-organic framework
3D continuous ion transport networks
Enhanced mechanical strength
Homogeneous Li-ion flux

ABSTRACT

The urgent need for high-energy and high-safety batteries is leading research to all-solid-state lithium-metal batteries. However, achieving high ionic conductivities, homogenous Li^+ flux, excellent interfacial compatibility, as well as enhanced mechanical strength simultaneously still remain a serious challenge for solid-state electrolyte (SSE). Herein, we rationally develop a three-dimensional (3D) interconnected metal-organic framework (MOF) network-based SSE without any liquid, where the MOF with optimized pore size and strong cationic site is able to restrict anions transport to afford a homogeneous Li^+ flux and a high Li^+ transference number (0.52). Furthermore, the 3D interconnected MOF-based networks not only build continuous ion conductive pathways for fast Li^+ transport (ionic conductivity of 2.89×10^{-4} S cm^{-1}), but also provide structural reinforcement to enhance the mechanical strength (Young's modulus of 819.4 MPa). Consequently, the Li||Li symmetric cell using 3D interconnected MOF-derived SSE can be stably operated for more than 700 h. The all-solid-state lithium-metal full cells fabricated with 3D interconnected MOF-derived SSE exhibit excellent cycling performance even with a 20 μm thin Li anode or high-voltage cathode.

1. Introduction

Lithium-ion batteries (LIBs) have become the dominant energy storage devices owing to their high energy and power densities, low self-discharge rates and long cycle lives [1–3]. To fulfill the ever-growing demand for higher energy density systems, the lithium metal has been recognized as an ultimate anode because of its high theoretical capacity and lowest redox potential [4–6]. Unfortunately, traditional organic liquid electrolyte cannot only spontaneously react with lithium metal generating unfavorable and thick interphases, but also lead to the formation of lithium dendrites because of uneven lithium deposition during electrochemical lithium plating and stripping. The lithium dendrites will subsequently penetrate the separator and cause internal short circuit, resulting in fire tragedies when encounter with highly volatile and flammable organic liquid electrolytes [7,8].

Replacing the flammable liquid electrolytes with solid-state electrolytes (SSEs) has been considered as the most promising approach for eliminating safety concerns in lithium-metal batteries, which was attributed to the fact that SSEs can overcome the intrinsic drawbacks of liquid electrolytes (i.e., leakage, volatility, and flammability) as well as effectively suppress the growth of lithium dendrite [9,10].

Normally, SSEs can be classified into three categories: inorganic solid electrolytes, solid polymer electrolytes (SPEs), and their composites [10–14]. Inorganic solid electrolytes, such as oxides (e.g., $Li_7La_3Zr_2O_{12}$, LLZO) and sulfides (e.g., Li_6PS_5Cl), generally possess high ionic conductivity, some of which even exceeds that of liquid electrolytes (e.g., 25 mS cm^{-1} for $Li_{9.54}Si_{1.74}P_{1.44}S_{11.7}Cl_{0.3}$) [15]. However, inorganic solid electrolytes suffered from fragility, air instability, and large interfacial impedance. SPEs, such as poly(ethylene oxide) (PEO) and poly(vinylidene fluoride) (PVDF), promise lightweight, high flexibility, and low interfacial impedance, while their low ionic conductivity and poor mechanical strength restrain their practical applications [16,17].

Introducing inorganic fillers into the polymer matrix to form composite solid electrolytes (CSEs) is considered to be the most effective strategy to boost the performance of lithium batteries because it combines the advantages of inorganic and polymer electrolytes while overcoming their disadvantages [10,13,14,18–21]. Unfortunately, their simple combination often cannot provide sufficient improvement in Li^+ conductivity, which may be ascribed to the fact that those inorganic fillers tend to aggregate at increased content as well as fail to form a continuous Li^+ transport pathway. Thus, a great deal of research efforts has been carried out to construct continuous pathway for Li^+ transfer in CSEs [22–28]. For instance, Fu et al. first fabricated a three-dimensional (3D) Li^+–

* Corresponding authors.
E-mail addresses: caiyp@scnu.edu.cn (Y.-p. Cai), qifeng.zheng@m.scnu.edu.cn (Q. Zheng).
[1] These authors contributed equally to this work.

https://doi.org/10.1016/j.ensm.2022.02.014
Received 3 January 2022; Received in revised form 7 February 2022; Accepted 8 February 2022
Available online 10 February 2022

conducting LLZO network through electrospinning and then backfilled with polymer electrolyte to provide continuous Li^+ transfer pathways in CSE [23]. Such a 3D interconnected LLZO network not only effectively increases the ionic conductivity, but also provides structural reinforcement to enhance the mechanical strength of CSE. Later on, Li et al. reported a 3D $Li_{1.4}Al_{0.4}Ti_{1.6}(PO_4)_3$ (LATP)/polyacrylonitrile (PAN) fiber network reinforced CSE, in which the continuous fiber network contributes to the enhancement of both mechanical strength and ionic conductivity, as well as inhibits the chemical reaction between LATP and lithium metal [22]. Nevertheless, the growth of lithium dendrites still occurs, especially at grain boundaries, due to the inhomogeneous Li electrochemical deposition.

Metal-organic frameworks (MOFs) are a fast-growing type of crystalline porous inorganic-organic materials assembled by metal ions or inorganic clusters and organic ligands, which hold great potential for application in CSEs owing to their intrinsic merits [29–33]. First of all, the high specific surface areas of MOFs not only allows for closely packed Li^+ hopping sites that minimizes activation energy for ion transport, but also facilitate their contact with other components in CSEs that reduces interfacial resistance. Secondly, the pore sizes of MOFs can be tuned to cage the anions and the unsaturated metal sites of MOFs can coordinate with anions, which would promote Li^+ transfer, thereby increasing the Li^+ transference number and ionic conductivity [34]. Last but not least, the periodical crystalline structure and ordered channels of MOFs offer a homogeneous Li^+ flux that leads to homogeneous Li^+ electrodeposition during the charging-discharging process, preventing the growth of lithium dendrites [35]. For instance, Huo et al. fabricated a cationic MOF/polymer CSE, of which the cationic MOF with high surface area could effectively immobilize anions via electrostatic interaction that leads to high Li^+ transference number and uniform Li^+ deposition [30]. However, achieving fast ion transport, homogeneous Li^+ flux, excellent interfacial compatibility, and enhanced mechanical strength simultaneously still remains a critical challenge for CSEs.

Herein, we rationally developed an interconnected MOFs network-based CSE to address the above challenge, which was fabricated by constructing 3D interconnected MOFs network *via* electrospinning and then backfilled with polymer/lithium salt. As illustrated in Scheme 1, the construction of 3D interconnected MOF/PAN network not only provides a continuous pathway for fast Li^+ transport between MOF particles thereby effectively increasing the ionic conductivity, but also significantly enhances the mechanical strength of the resulting CSE owing to the reinforcement of 3D network. Meanwhile, MOFs with ordered structure, appropriate pore size, and strong cationic site were chosen as to restrict anion transport afford a uniform distribution of Li^+ flux, which increases the Li^+ transference number and leads to the homogeneous deposition of Li^+, thereby inhibiting the growth of lithium dendrite. The physicochemical and electrochemical properties of the 3D interconnected MOFs network-based CSE were carefully examined, showing great promise for applications in high-energy-density and high safety solid-state lithium metal batteries.

2. Experimental section

2.1. Fabrication of 3D-UIO-66/PAN nanofiber network

The synthesized UIO-66 (Zirconium benzenedicarboxylate MOF) particles and PAN powder were added to DMF solvent, of which the mixture was first subjected to sonication for 30 min and then stirred magnetically for 12 h to obtain a homogeneous solution. The mass ratio of UIO-66, PAN, and DMF was 1:1:10. A high voltage of 10 kV was applied during the electrospinning process, and the aluminum foil was used as collector and placed in a fixed distance of 15 cm from the needle to collect the spun nanofiber with a three-dimensional network (i.e., 3D-UIO-66/PAN nanofiber network). The as-spun 3D-UIO-66/PAN nanofiber network was peeled off from the aluminum collector and dried at 150 °C under vacuum for 24 h to remove the residual solvent. For comparison, the nanofiber network with a different UIO-66: PAN ratio of 2:3 (i.e., 3D-2UIO-66/3PAN), as well as the nanofiber network with different types of MOFs (i.e., 3D-ZIF-8/PAN and 3D-MOF-74/PAN) were also prepared using the same procedure, where ZIF-8 is zeolitic imidazolate framework-8 and MOF-74 is cobalt 2,5-dihydroxyterephthalic MOF.

2.2. Fabrication of 3D-UIO-66/PAN/PEO/LiTFSI CSE

PEO and LiTFSI (the molar ratio of ethylene oxide [EO] to LiTFSI was 18:1) were dissolved in acetonitrile with a concentration of 4.0 wt.% of PEO, of which the mixture was then vigorously stirred for 12 h to obtain PEO/LiTFSI solution. Then, the PEO/LiTFSI solution was dropped on 3D-UIO-66/PAN nanofiber network and then subjected to a vacuum-assisted liquid filling method. The wetting and vacuum process was repeated several times to make sure the 3D-UIO-66/PAN nanofiber network was fully infiltrated with PEO/LiTFSI. The resulting composite membrane was then dried in a vacuum oven at 150 °C for 24 h to obtain 3D-UIO-66/PAN/PEO/LiTFSI CSE. The 3D-UIO-66/PAN/PEO/LiTFSI CSE was the transferred to glove box and further dried at 80 °C for 3 days prior to use. For comparison, the 3D-2UIO-66/3PAN/PEO/LiTFSI, 3D-ZIF-8/PAN/PEO/LiTFSI, and 3D-MOF-74/PAN/PEO/LiTFSI CSEs were fabricated using the same procedure. The PEO/LiTFSI SSE was prepared by simply casting the PEO/LITFSI solution on glass, the UIO-66/PEO/LiTFSI SSE was prepared by physically mixing the UIO-66 particles into PEO/LiTFSI solution, followed by casting the mixture on glass. The 3D-PAN/PEO/LiTFSI SSE was prepared by backfilling the 3D-PAN nanofiber network with PEO/LiTFSI solution.

2.3. Preparation of the electrodes

Using a Thinky (AR-100) mixer, the cathode (i.e., LFP or NMC) was fabricated by mixing LFP or NMC powder with acetylene black (AB, Denka Black) and polyvinylidene difluoride (PVDF, Kynar) in N-methyl-2-pyrrolidone (NMP) at a weight ratio of 80: 12: 8. The slurry was then coated on an aluminum foil and dried in a vacuum oven at 100 °C for at least 24 h. The active mass loading of LFP or NMC was controlled at 3,4 mg cm^{-2}.

2.4. Material characterization

To study the crystalline phases, the X-ray powder diffraction patterns were collected using a diffractometer (D8 Advance, Bruker) with Cu Kα radiation. The morphologies and microstructures were investigated using a scanning electron microscope (SEM, MAIA3, TESCAN Brno, s.r.o.). The mechanical properties of the SSEs were evaluated using a universal testing machine (Labthink XLW(PC)). The SSEs were cut into strips of 40 mm × 15 mm × 0.1 mm, and the testing rate was set at 25 mm min^{-1}. The chemical compositions of the Li metal electrode were analyzed using XPS (PerkinElmer PHI 1600 ESCA).

2.5. Electrochemical measurements

Using an Ar-filled glove box, all the cells including Li||Li, Li||SS, SS||SS, Li||LFP, and Li||NMC were assembled in a standard 2032 coin-cell configuration without adding any liquid electrolyte. The ionic conductivities of the SSEs were measured by AC impedance spectrum using a Potentiostat (VMP3, Bio-Logic). The SSEs were sandwiched between two stainless-steel (SS) blocking electrodes, and the electrochemical impedance spectra were collected at the temperature ranging from 303 to 333 K with an amplitude of 10 mV within the frequency ranging from 10^6 to 0.1 Hz. The ion conductivity (σ) of SSE was calculated according to the following equation,

$$\sigma = \frac{R}{L \times S} \tag{1}$$

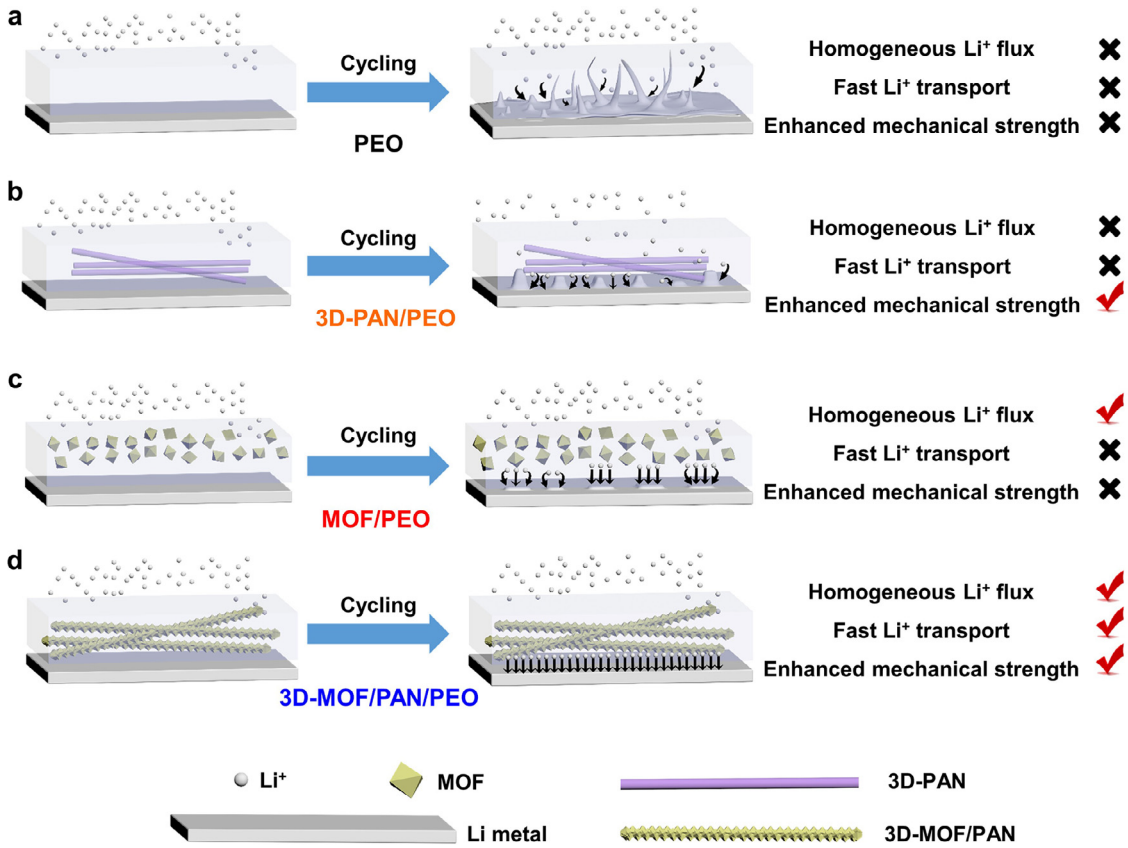

Scheme 1. Rational design of the 3D interconnected MOFs-based SSE. Schematic illustration of Li dendritic growth in (a) PEO/LiTFSI SSE, (b) 3D-PAN/PEO/LiTFSI SSE, (c) MOF/PEO/LiTFSI SSE and (d) 3D-MOF/PAN/PEO/LiTFSI SSE. Solid polymer electrolytes, such as PEO, have good interfacial compatibility, but suffer from low ionic conductivity, poor mechanical strength and lithium dendrite growth. The construction of 3D-PAN fiber network could significantly reinforce the mechanical strength, and the introduction of optimized MOFs with ordered structure could lead to the homogeneous deposition of Li^+. Thus, by constructing an 3D-MOF/PAN network, the resulting 3D interconnected MOFs-based CSEs not only possess enhanced mechanical strength and homogeneous deposition of Li^+, but also build continuous pathways for fast Li^+ transport.

where L is the thickness of SSE, R is the bulk resistance, and S is the area of SSE.

The electrochemical potential window of SSE was examined using a SS as the working electrode and lithium metal as both the reference and counter electrodes by linear sweep voltammetry (LSV) test at a sweep rate of 1.0 mV s^{-1} from open circuit voltage (OCV) to 6.0 V. The Li^+ transference number ($t_{Li}{}^+$) were measured according to the AC impedance and direct-current (DC) polarization (with a polarization voltage of 10 mV) using a symmetric Li||Li cell. The $t_{Li}{}^+$ was calculated from Bruce-Vincent-Evans equation,

$$t_{Li^+} = \frac{I_S \times (\Delta V - I_0 R_0)}{I_0 \times (\Delta V - I_S R_S)} \quad (2)$$

where ΔV is the applied polarization voltage ($\Delta V = 10$ mV), I_0 and R_0 are the initial current and charge-transfer resistance before polarization, respectively, and I_s and R_s are the steady state current and charge-transfer resistance after polarization for 7200 s, respectively.

All the charge-discharge tests were performed using a M340A charge-discharge tester (Wuhan Land, China). All the cells were kept at a temperature of 60 °C for 24 h prior to test. Li||Li symmetric cell were cycled in the galvanostatic mode with a current density of 0.3 mA cm^{-2} for 1 h at each plating or stripping cycle. The cycling performance and rate capability of Li||LFP and Li||NMC cells were tested with voltage ranges of 2.8–3.8 V and 2.8–4.3 V, respectively. For the thin Li||LFP cell, a thin Li foil of 20 μm was used as anode.

3. Results and discussion

3.1. Rationalization of the 3D interconnected MOFs-derived SSEs

As has been previously demonstrated, the crystalline MOFs with ordered channels intrinsically hold great promise for offering desirable molecular/ionic sieving/transport properties. Introducing the MOF with appropriate pore size and strong cationic site into SSE may be able to restrict the anion transport, which will offer a uniform distribution of Li^+ flux that enable homogeneous Li^+ electrodeposition (Scheme 1). Thus, considering the size of bis(trifluoromethane)sulfonimide anion ($TFSI^-$, 7.9 Å), the well-known UIO-66 ($Zr_6O_4(OH)_4(BDC)_6$, BDC=1,4-benzenedicarboxylate, Fig. 1a) with strong cationic site and slight bigger pore size (8.1 Å, respectively) than that of $TFSI^-$ anion, were chosen among thousands of reported MOFs. For comparison purpose, the ZIF-8 ($Zn(mIm)_2$, mIm=2-Methylimidazole, Fig. 1b) with smaller pore size of 4.2 Å as well as MOF-74 (Co_2(dobdc), dobdc=1,4-dioxido-2,5-benzenedicarboxylate, Fig. 1c) with bigger pore size of 11.3 Å were also systematically investigated.

To demonstrate the interaction between the cationic site of MOF and $TFSI^-$ anion, the adsorption energy is calculated based on density functional theory (DFT). The $TFSI^-$ anion was placed either on the surface or inside the channel of MOF. As shown in Fig. 1, the UIO-66 has an adsorption energy of −1.70 eV and −0.63, respectively with $TFSI^-$ anion on the surface and inside the channel, which is much higher than that of ZIF-8 and MOF-74, suggesting a strong interaction between UIO-66 and $TFSI^-$ anion. Three types of MOFs were synthesized *via* hydrothermal

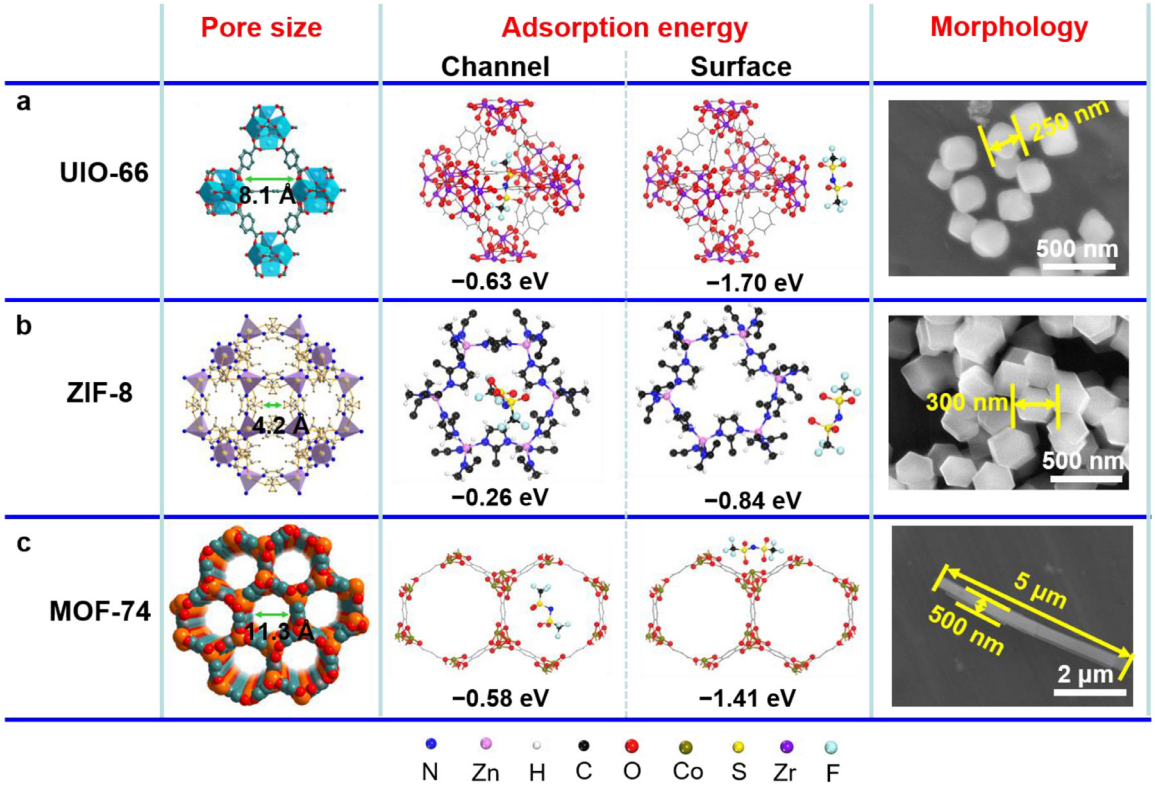

Fig. 1. Rationalization of the MOFs. The crystalline structures and SEM images of (a) UIO-66, (b) ZIF-8, and (c) MOF-74, which clearly show their differences in pore sizes, adsorption energies with $TFSI^-$, and morphologies.

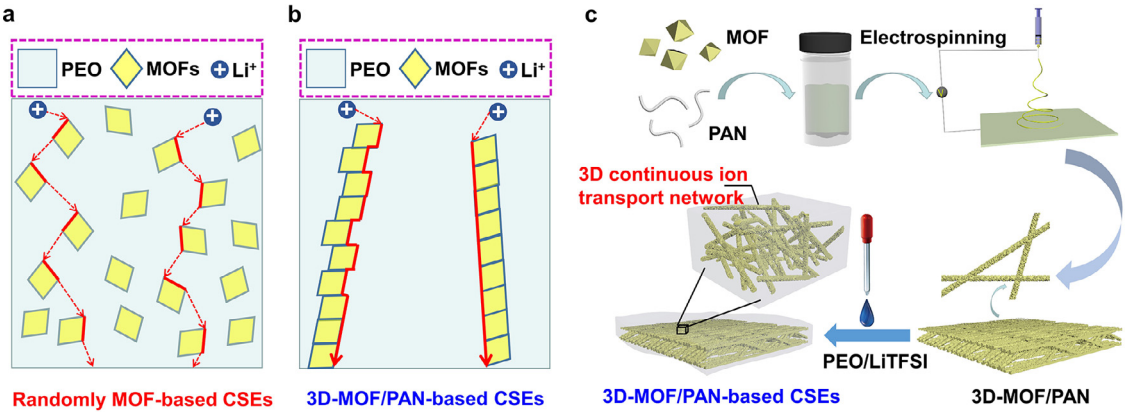

Fig. 2. Fabrication procedure and its ion transport pathways of a 3D interconnected MOF/PAN-based CSE. Schematic illustrations of Li^+ transport pathways for (a) randomly distributed MOF-based CSEs and (b) 3D interconnected MOFs-based CSEs. (c) Schematic procedure to fabricate 3D interconnected MOFs-based CSEs. The 3D interconnected MOF/PAN network was prepared by electrospinning the mixture solution of MOFs and PAN. Subsequently, the 3D interconnected MOF/PAN network was backfilled with PEO/LiTFSI solution to produce 3D-MOF/PAN-based CSEs with continuous ion transport network and enhanced mechanical strength.

reaction and their morphologies (Fig. 1) as well as crystalline structures (Fig. S1) were carefully investigated. UIO-66 with the most ideal pores and strongest adsorption energies with $TFSI^-$ anion were expected to restrict the $TFSI^-$ anion transport, leading to the improvement of Li^+ transference number ($t_{Li}{}^+$).

As shown in the Fig. 2a, for the randomly dispersed MOF-based CSE, the contact between MOF particles is loose, the Li^+ has to migrate across the MOF-to-PEO-to-MOF, which consequently makes the improvement of ionic conductivity very limit. Therefore, aiming to form closer contacts and build continuous ion transport pathways between MOF particles (Fig. 2b), a 3D interconnected MOF/PAN fiber network was first prepared by electrospinning and then backfilled with a PEO/lithium bis(trifluoromethane)sulfonimide (LiTFSI) solution to produce 3D-MOF/PAN-based CSEs (Fig. 2c), where the MOF-to-MOF ion transport pathways were built. Compared with the CSEs prepared by randomly adding MOFs to polymer electrolytes (Fig. 2a), the as-designed 3D-MOF/PAN-based CSEs not only promise the enhanced mechanical strength and homogeneous deposition of Li^+ that effectively hinders the growth of lithium dendrites, but also provide a continuous pathway for fast Li^+ transport that increasing the ionic conductivity and Li^+ transference number (Fig. 2b).

As shown in Fig. 3a, the 3D-UIO-66/PAN nanofibers prepared *via* electrospinning exhibits a diameter of ~ 0.9 μm, where the UIO-66 nanoparticles are evenly distributed on the nanofiber as well as highly interconnected with each other (i.e., without intervals), which is beneficial to build continuous ion transport pathways and thereby promoting

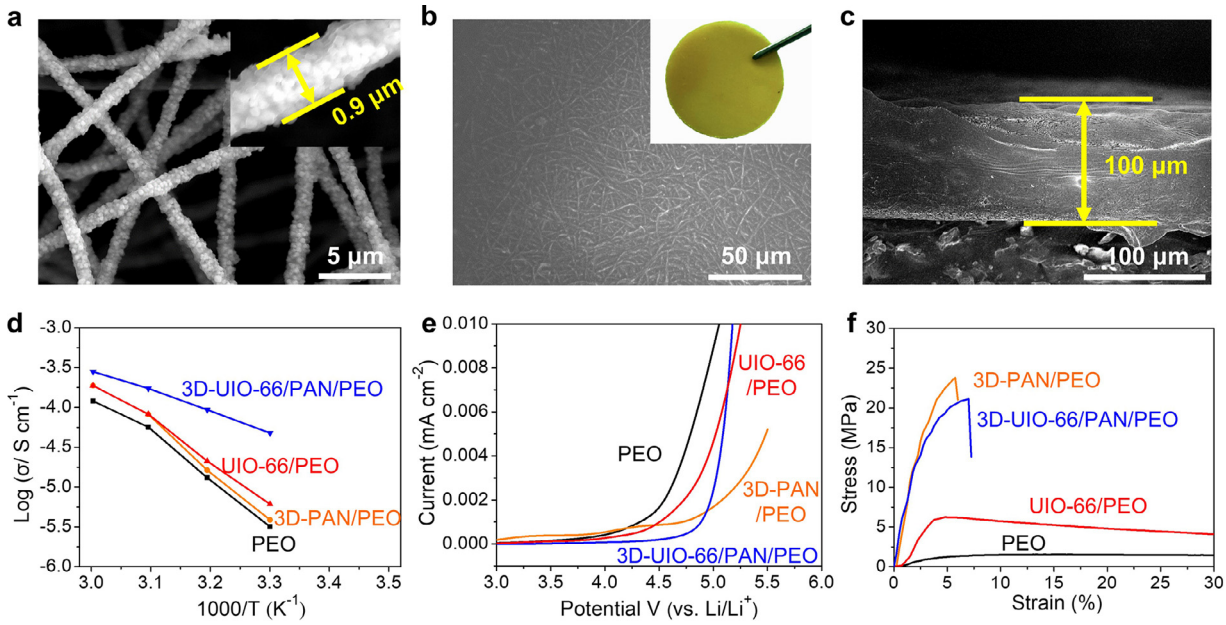

Fig. 3. Characterizations of the SSEs. SEM images of (a) an interconnected 3D-UIO-66/PAN network fabricated by electrospinning, (b) top and (c) cross-sectional view of an interconnected 3D-UIO-66/PAN/PEO CSE after backfilled with PEO/LiTFSI. (d) Temperature-dependent ionic conductivities, (e) oxidative stabilities, and (f) stress-strain curves of the PEO/LiTFSI, 3D-PAN/PEO/LiTFSI, UIO-66/PEO/LiTFSI and 3D-UIO-66/PAN/PEO/LiTFSI SSEs.

Li^+ transport. In order to obtain the uniform and interconnected 3D-UIO-66/PAN nanofiber, the mass ratio of UIO-66 and PAN in the precursor solution was optimized to be 1: 1 and applied through this study, unless otherwise specified. The uniform distribution of UIO-66 in the 3D network was further confirmed by the energy dispersive X-ray spectroscopy (EDS) mapping images (Fig. S2). Fig. S3 shows the SEM image of 3D-UIO-66/PAN nanofiber with a UIO-66: PAN mass ratio of 2: 3 (abbreviated as 3D-2UIO-66/3PAN), where the UIO-66 particles were not connected with each other to form continuous ion transport pathways.

After backfilling with a PEO/LiTFSI solution, a highly flexible and free-standing 3D-UIO-66/PAN/PEO/LiTFSI CSE membrane with a thickness of ~ 100 μm was obtained, of which the 3D-UIO/PAN network was fully infiltrated with PEO/LiTFSI (Fig. 3b and c). Since rigorous drying protocol was applied during the fabrication, we assume that the 3D-UIO-66/PAN/PEO/LiTFSI CSE prepared in this study do not contain any liquid, which was verified by the negligible weight loss before 200 °C during the thermogravimetric analysis (TGA) test (Fig. S4). The X-ray diffraction (XRD) patterns of 3D-UIO-66/PAN/PEO/LiTFSI CSE membrane is consistent with that of 3D-UIO-66/PAN nanofiber and pristine UIO-66 nanoparticles (Fig. S5), implying that it can maintain the intrinsic crystallinity after the electrospinning and backfilling process. For comparison, the PEO-based electrolyte (i.e., PEO/LiTFSI), the 3D-PAN nanofiber reinforced PEO-based electrolyte (i.e., 3D-PAN/PEO/LiTFSI), and UIO-66 physical mixed PEO-based electrolyte (i.e., UIO-66/PEO/LiTFSI) with a similar thickness of ~ 100 μm were also fabricated (Fig. S6).

3.2. Physical and physicochemical properties of the SSEs

The ionic conductivity of a SSE is a prerequisite parameter for its practical application in batteries, which was calculated from the AC impedance spectrum of SSE sandwiched between stainless steel (SS) blocking electrodes. The ionic conductivities and selected electrochemical impedance spectra are shown in Figs. 3d and S8, the 3D-UIO-66/PAN/PEO/LiTFSI SSE without any liquid exhibits an ionic conductivity of 4.87×10^{-5} S cm^{-1} at 30 °C, which is one order of magnitude higher than that of PEO/LiTFSI (3.18×10^{-6} S cm^{-1}), 3D-PAN/PEO/LiTFSI (3.88×10^{-6} S cm^{-1}), and UIO-66/PEO/LiTFSI (6.10×10^{-6} S cm^{-1}) SSEs. The ionic conductivities of all SSEs gradually increase with increasing temperature, and reach at 2.89×10^{-4} S cm^{-1} for the 3D-UIO-66/PAN/PEO/LiTFSI CSE at 60 °C. Furthermore, according to the Arrhenius equation, the activation energies (E_a) of various CSEs were derived from Fig. 3d. The E_a of the 3D-UIO-66/PAN/PEO/LiTFSI CSE is calculated to be 0.20 eV, which is much lower than that of PEO/LiTFSI (0.43 eV), 3D-PAN/PEO/LiTFSI (0.46 eV), and UIO-66/PEO/LiTFSI (0.40 eV) CSEs, indicating that lower energy barrier is needed for Li^+ migration in 3D-UIO-66/PAN/PEO/LiTFSI CSE. The dramatic increase in ionic conductivity and reduce in migration barrier are attributed to the fact that the UIO-66 particles with strong cationic sites were highly interconnected with each other *via* electrospinning, which forms continuous ion transport pathway (Fig. 2b), leading to the fast ion transport. It is necessary to emphasize that the UIO-66/PEO/LiTFSI CSE (i.e., physically mixing UIO-66 with polymer) with the same content of UIO-66 particles shows a much poorer ionic conductivity and higher migration barrier, due to the bare contact between the UIO-66 particles and thus unable to form continuous ion transport pathway (Fig. 2c), making the Li-ion transport becomes challenging.

The electrochemical stability window of SSEs is an important criterion for their application in high-voltage batteries, which was evaluated by linear sweep voltammetry (LSV) at room temperature. As shown in Fig. 3e, the 3D-UIO-66/PAN/PEO/LiTFSI CSE showed a high oxidation potential of 4.7 V defined at 0.5 μA cm^{-2}, which is much higher than that of the PEO/LiTFSI (4.0 V), 3D-PAN/PEO/LiTFSI (3.9 V), and UIO-66/PEO/LiTFSI (4.3 V) CSEs. The high oxidative stability of the 3D-UIO-66/PAN/PEO/LiTFSI CSE was attributed not only to the intrinsically high voltage tolerance of the UIO-66 filler itself, but also primarily to the continuous ion transport pathways offered by the highly interconnected 3D-UIO-66/PAN fiber network, which minimizes the migration of charge (i.e., Li^+) in the PEO polymer matrix and therefore postpones the oxidation of PEO.

Fig. 3f shows the stress-strain curves of the various SSEs investigated in this study. The 3D-UIO-66/PAN/PEO/LiTFSI CSE exhibits a high Young's modulus of 819.4 MPa, which is much higher than that of the PEO/LiTFSI (15.6 MPa) and UIO-66/PEO/LiTFSI (159.0 MPa) CSEs, as well as slightly higher than that of 3D-PAN/PEO/LiTFSI (643.7 MPa). The mechanical property of the 3D-UIO-66/PAN/PEO/LiTFSI CSE also outperforms most of state-of-the-art reported SSEs (Table S1). The en-

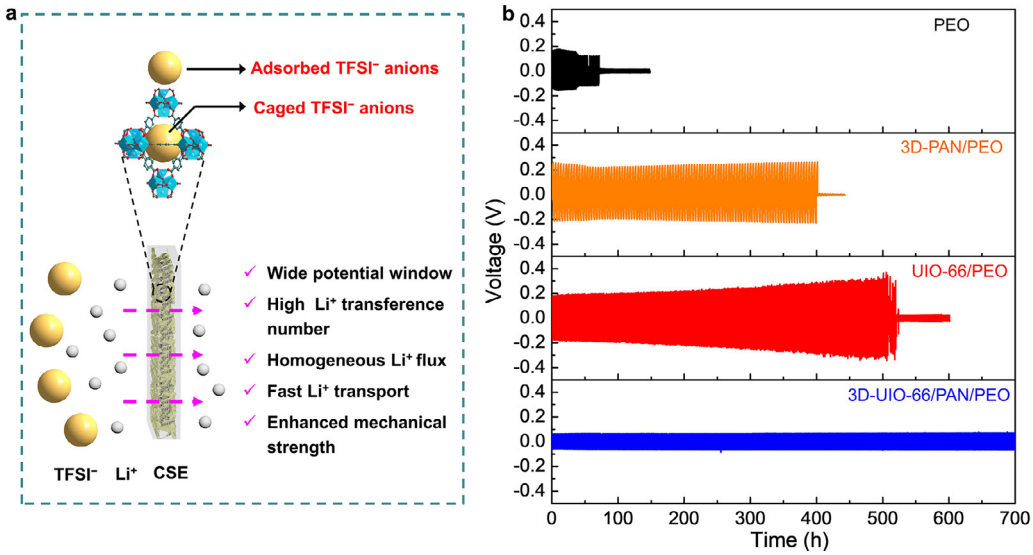

Fig. 4. Representation of a 3D-UIO-66/PAN/PEO/LiTFSI CSE in the application of a Li-metal battery. (a) Schematic illustration of ion transport through an interconnected 3D-UIO-66/PAN/PEO/LiTFSI CSE, where the $TFSI^-$ anions were restricted by UIO-66, leading to homogeneous Li^+ flux and high Li^+ transference number; (b) long-term cycling stabilities of symmetric Li||Li cells using PEO/LiTFSI, 3D-PAN/PEO/LiTFSI, UIO-66/PEO/LiTFSI and 3D-UIO-66/PAN/PEO/LiTFSI SSEs at a current density of 0.3 mA cm^{-2} for 0.3 mAh cm^{-2} at 60 °C.

hanced mechanical strength is attributed to the reinforcement of 3D-UIO-66/PAN nanofiber networks, which will be beneficial for suppressing the growth of lithium dendrites physically during electrochemical plating.

Furthermore, Li^+ transference number ($t_{Li}{}^+$) is an important factor to evaluate the mobility of Li^+, of which high $t_{Li}{}^+$ will enable the fast charge-discharge of batteries, while low $t_{Li}{}^+$ will build large Li^+ concentration gradient near the lithium anode and thus form a strong interfacial electric-field, thereby causing the growth of lithium dendrites [36,37]. The $t_{Li}{}^+$ was calculated according to the AC impedance and direct-current (DC) polarization. As shown in Figs. S11 and S12, the $t_{Li}{}^+$ of the 3D-UIO-66/PAN/PEO/LiTFSI CSE is calculated to be 0.52, which is much higher than that of the PEO/LiTFSI (0.17), 3D-PAN/PEO/LiTFSI (0.18), UIO-66/PEO/LiTFSI (0.25), and 3D-2UIO-66/3PAN/PEO/LiTFSI (0.26) CSEs. As shown in Fig. 4a, the high $t_{Li}{}^+$ of 3D-UIO-66/PAN/PEO/LiTFSI CSE can be attributed to the following three reasons: (1) the UIO-66 has a pore size of 8.1 Å that is slightly bigger than that of $TFSI^-$ anion (7.9 Å), which effectively restricts the transport of $TFSI^-$ anion; (2) the transport of $TFSI^-$ anion was further restricted by the strong absorption capability of UIO-66; (3) the continuous Li^+ transport pathways offered by highly interconnected 3D-UIO-66/PAN nanofiber networks in CSE also contribute to the rapid migration of Li^+. In contrast, the 3D-ZIF-8/PAN/PEO/LiTFSI and 3D-MOF-74/PAN/PEO/LiTFSI SSEs showed a $t_{Li}{}^+$ of 0.42 and 0.26, (Fig. S13), respectively, which was due to the unmatched pore size and lower adsorption energy that allows $TFSI^-$ anion to migrate easily.

3.3. Homogeneous Li deposition

As schematically summarized in Fig. 4a, through rational design of highly interconnected MOF-derived CSE, namely, MOF with appropriate pore size and strong cationic site, the interconnected MOF-based nanofiber with continuous Li^+ transport pathways, as well as nanofiber network with structural reinforcement, the resulting 3D-UIO-66/PAN/PEO/LiTFSI CSE not only has wide potential window, high Li^+ transference number and enhanced mechanical strength, but also enables fast Li^+ transport and homogeneous Li^+ deposition, which makes it very attractive and promising for application in solid lithium metal batteries.

The Li||Li symmetric cells using various SSEs were fabricated to evaluate the long-term electrochemical stabilities and polarization during Li plating and stripping process. The cycling tests were carried out at 60 °C with a current density of 0.3 mA cm^{-2} after 3 activation cycles of 0.1 mA cm^{-2} with each plating/stripping procedure of 1 h. As shown in Fig. 4b, the Li||Li cell using PEO/LiTFSI SSE experienced a hard short after only 80 h due to overgrowth of the lithium dendrites, while the cycling life was extended to about 400 h for that of using 3D-PAN/PEO/LiTFSI, which was attributed to the enhanced mechanical strength offered by 3D-nanofiber reinforced structure that can suppress dendrite formation (Scheme 1 and Fig. 3f). Meanwhile, since the UIO-66 can cage and adsorb the $TFSI^-$ anion that results in a homogenous Li^+ flux, the Li||Li cell using UIO-66/PEO/LiTFSI SSE can sustain the homogenous deposition of Li^+ for about 500 h (Scheme 1 and Fig. 4a). Remarkably, benefiting from the high Li^+ transference number, enhanced mechanical strength, fast Li^+ transport as well as homogenous Li^+ flux offered by the highly interconnected 3D-UIO-66/PAN network, the Li||Li cell using 3D-UIO-66/PAN/PEO/LiTFSI CSE exhibited an extraordinarily stable cycling performance with a very small and smooth polarization (Voltage: ~65 mV), and no short-circuit appeared even after 700 h.

As revealed by the COMSOL simulation, the 3D-UIO-66/PAN/PEO/LiTFSI CSE exhibited small concentration gradients for both Li^+ and $TFSI^-$ during Li deposition (Fig. 5a and b), indicating the formation of homogeneous Li^+ flux. This results in a negligible electric potential field (Fig. 5c), which is beneficial to realize uniform Li deposition and long cycling. In contrast, ascribing to the low $t_{Li}{}^+$, the UIO-66/PEO/LiTFSI CSE presented much larger concentration gradients for both Li^+ and $TFSI^-$ than that of 3D-UIO-66/PAN/PEO/LiTFSI CSE (Fig. 5d and e), which induces a large electric potential field (Fig. 5f) and consequently leads to the inhomogeneous Li deposition and dendrite growth.

In addition to the homogeneous Li^+ flux offered by the 3D-UIO-66/PAN/PEO/LiTFSI CSE, the interfacial chemistry also plays a significant role in regulating Li deposition, which was investigated by X-ray photoelectron spectroscopy (XPS). As shown in the Fig. S16, the surface of the cycled Li metal is enriched with LiF, Li_3N, $-CF_3$, and sulfur compounds, of which those inorganic interfacial components have been demonstrated to help stabilize the interface and offer better Li cyclability [38–40].

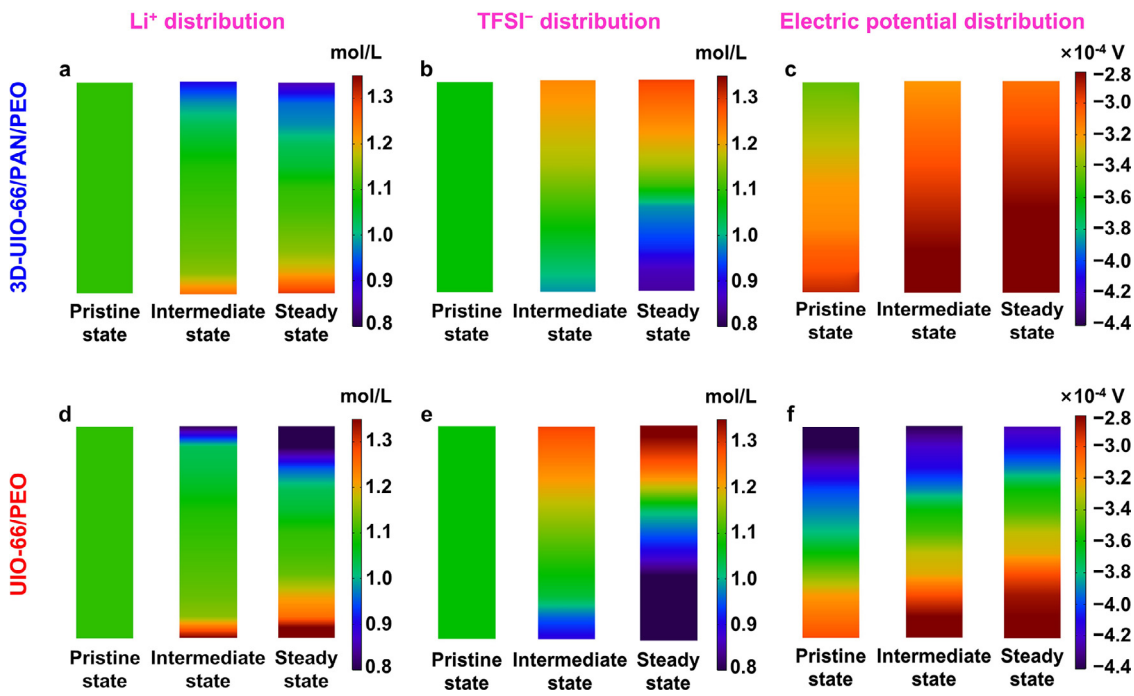

Fig. 5. COMSOL simulation of Li^+, $TFSI^-$, and electric potential distribution in (a–c) 3D-UIO-66/PAN/PEO/LiTFSI CSE and (d–f) UIO-66/PEO/LiTFSI CSE at pristine, intermediate, and steady state during Li deposition at a current density of 0.3 mA cm^{-2}.

3.4. Stable operation of 20 μm thin Li||LFP and high voltage Li||NMC cells

To demonstrate the merits of constructing 3D interconnected MOF-derived network in CSE, the solid-state Li metal cells with $LiFePO_4$ (LFP) cathode using various SSEs were assembled and their electrochemical performances were tested at 60 °C. As shown in Fig. 6a, the Li||LFP cell using 3D-UIO-66/PAN/PEO/LiTFSI CSE delivered excellent rate capability, which high capacities of 160, 162, 158, and 152 mAh g^{-1} at 0.1, 0.2, 0.5, and 1 C were retained, respectively. In contrast, the Li||LFP cells using PEO/LiTFSI, 3D-PAN/PEO/LiTFSI, and UIO-66/PEO/LiTFSI SSEs showed similar capacities at low C rate of 0.1 C, while their capacities decreased dramatically at high C rates. For instance, the cell using PEO/LiTFSI SPE were not able to deliver any valid capacity when charging rate larger than 0.5 C. Furthermore, the Li||LFP cell using 3D-UIO-66/PAN/PEO/LiTFSI exhibited very low overpotentials (e.g., ~110 mV at 0.5 C), which was much lower than of using other types of SSEs, owing to the high ionic conductivity and Li^+ transference number of 3D-UIO-66/PAN/PEO/LiTFSI SSE (Figs. 6b and S17).

To further reveal the advantages of the 3D-UIO-66/PAN/PEO/LiTFSI SSE in guiding the homogeneous deposition of Li, a 20 μm thin Li foil was used to assemble the thin Li||LFP cell (N/P ratio of ~6), which exhibited a very stable cycling performance with a high capacity retention of 86% and a high average Coulombic efficiency (CE) of 99.8% after 300 cycles at 0.2 C (Fig. 6c). Furthermore, no obvious increase in voltage polarization in the charge-discharge curves was observed (Fig. S18), and their interfacial resistance remains stable (Fig. S19) during cycling, suggesting excellent interfacial compatibility towards both cathode and anode. In sharp contrast, the 20 μm thin Li||LFP cell using PEO/LiTFSI, 3D-PAN/PEO/LiTFSI, or UIO-66/PEO/LiTFSI SSE fails within 14, 31, and 128 cycles, respectively, with low CE (Fig. 6c).

The surface morphologies of the Li metal in 20 μm thin Li||LFP cells after cycling were investigated. For the cell using either PEO/LiTFSI or 3D-PAN/PEO/LiTFSI SSE, massive porous and dendritic Li were observed on the surface of Li metal (Fig. 6d and e), which leads to local short circuit during charging-discharging process. For the cell using UIO-66/PEO/LiTFSI SSE, massive porous and dendritic Li disappeared, but the Li surface is still a bit of rough (Fig. 6f), indicating that the UIO-66 particles could guide the uniform deposition of Li^+ and suppress the growth of lithium dendrites to some extent, but cannot resolve the issue thoroughly. Nevertheless, the Li metal in cycled Li||LFP cell using a 3D-UIO-66/PAN/PEO/LiTFSI SSE showed a smooth and shiny surface (Fig. 6g), demonstrating the growth of lithium dendrite can be effectively hindered. The superior performance offered by 3D-UIO-66/PAN/PEO/LiTFSI SSE can be attributed to the following three reasons: (1) the $TFSI^-$ anion transport was restricted by the angstrom-scale pores and strong cationic sites of UIO-66 that results in a homogenous Li^+ flux and high Li^+ transference number; (2) the highly interconnected UIO-66 nanofiber build continuous pathways for fast Li^+ transport between UIO-66 particles thereby effectively increasing the ionic conductivity; and (3) the 3D-UIO-66/PAN nanofiber networks significantly enhance the mechanical strength of the resulting CSE that could inhibit the growth of lithium dendrites.

Moreover, as shown in Fig. S20, the Li||LFP cell using 3D-UIO-66/PAN/PEO/LiTFSI SSE also demonstrated a stable cycling at a higher rate of 0.5 C, which retained 89% capacity with average CE of 99.9% over 300 cycles, which has never been achieved for other state-of-art reported MOFs/polymer based CSEs without any liquid (Table S2). Contrastingly, the cell using either PEO/LiTFSI, 3D-PAN/PEO/LiTFSI, or UIO-66/PEO/LiTFSI SSE cannot operate normally.

It is surprising to note that Li||LFP cell using a 3D-MOF-74/PAN/PEO/LiTFSI SSE also delivered a good capacity retention of 74% after 250 cycles (Fig. S21), even though both ionic conductivity and Li^+ transference number are relatively low for the 3D-MOF-74/PAN/PEO/LiTFSI SSE. This may be attributed to the tubular pore structure of MOF-74 that allows the Li^+ transport along the tube, which minimizes the Li^+ transport across different MOF particles. Based on these results, we encourage further investigation along these lines. For instance, constructing vertically aligned tubular MOFs (with appropriate pore size and strong cationic site) between cathode and anode would be expected to provide the shortest ion transport pathway and lowest ion migration barrier, which would boost the battery performance.

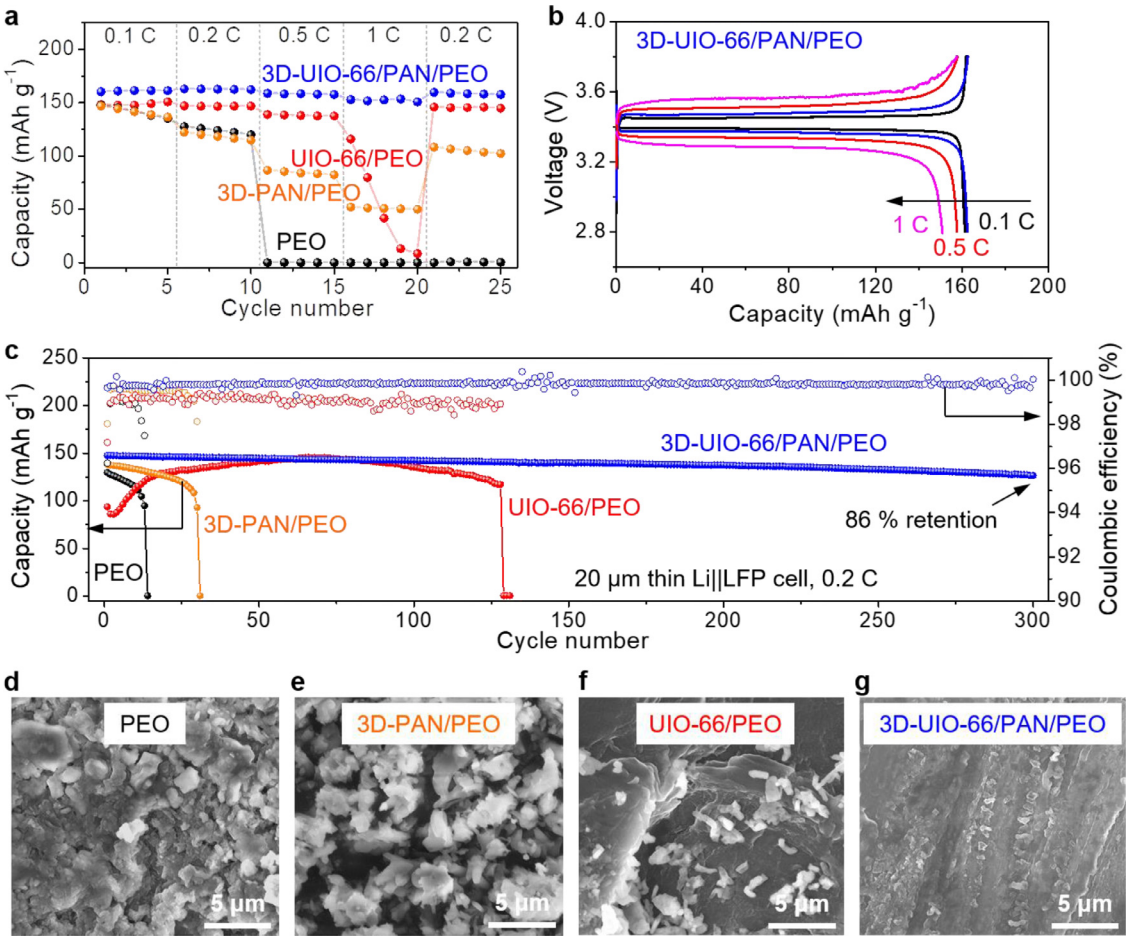

Fig. 6. Electrochemical performance of the Li||LFP cells at 60 °C. (a) Rate performance of Li||LFP cells using various SSEs; (b) charge-discharge curves of a Li||LFP cell using 3D-UIO-66/PAN/PEO/LiTFSI SSE at different charging rates; (c) cycling performance of 20 μm thin Li||LFP cells using PEO/LiTFSI, 3D-PAN/PEO/LiTFSI, UIO-66/PEO/LiTFSI and 3D-UIO-66/PAN/PEO/LiTFSI SSEs at 0.2 C after 3 formation cycles at 0.1 C; and the corresponding surface morphology images of the Li metal after cycling in (d) PEO/LiTFSI, (e) 3D-PAN/PEO/LiTFSI, (f) UIO-66/PEO/LiTFSI, and (g) 3D-UIO-66/PAN/PEO/LiTFSI SSEs. Note: the SEM images were collected at failure cycle for cells using PEO/LiTFSI (i.e., 14th cycle) and 3D-PAN/PEO/LiTFSI (i.e., 31th cycle) SSEs, while were collected after 100 cycles for cells using UIO-66/PEO/LiTFSI and 3D-UIO-66/PAN/PEO/LiTFSI SSEs.

In addition, benefiting from the wide potential window, the 3D-UIO-66/PAN/PEO/LiTFSI SSE also allows for a highly reversible charge-discharge for high voltage $LiNi_{1/3}Mn_{1/3}Co_{1/3}O_2$ (NMC) cathode testing from 2.8 to 4.3 V, which delivered a decent capacity retention of 57% after 100 cycles (Fig. S23).

It should be noted that there are some previous publication reported ionic conductivities and Li^+ transference numbers exceeding 1.0×10^{-3} S cm^{-1} and 0.6, respectively, for MOFs/polymer CSEs with the aid of organic solvent/ionic liquid [33,41,42]. For instance, Zhang et al. [33] crosslinked the UIO-66-OH with polymer and then soaked with 1.0 M LiTFSI in propylene carbonate (PC) solvent, the optimized CSE showed a high ionic conductivity of 1.70×10^{-3} S cm^{-1} and a high Li^+ transference number of 0.8 at 30 °C. Following the similar proceduare reported by Huang's group, by wetting our 3D-UIO-66/PAN/PEO/LiTFSI CSE with PC, the resulting PC-wetted 3D-UIO-66/PAN/PEO/LiTFSI CSE exhibited an extremely high ionic conductivity of 2.98×10^{-3} S cm^{-1} and a high Li^+ transference number of 0.68 at 30 °C, which enabled the stable cycling of Li||LFP for over 1000 cycles at a very high rate of 2C at 30 °C (Fig. S24), outperforming most of reported MOFs/polymer based CSEs with the aid of solvent or ionic liquid (Table S3). However, adding organic solvent/ionic liquid to boost the electrochemical performance is out of the scope of this study, since the main focus is to reveal the promising role of MOFs in realizing tunable ion transport as well as demonstrate the effectiveness and importance of constructing MOF-based 3D continuous ion transport networks in SSEs.

4. Conclusions

In summary, a highly interconnected MOFs-based CSE was fabricated by constructing a 3D interconnected MOFs network *via* electrospinning and then backfilled with polymer/lithium salt. The design rationale is that MOFs with ordered structure, carefully selected pore size and strong cationic site are able to restrict anions transport to afford a homogeneous distribution of Li^+ flux and a high Li^+ transference number, and the highly interconnected MOFs-based networks cannot only provide continuous ion conductive pathways for fast Li^+ transport, but also significantly enhance the mechanical strength. Therefore, the resulting 3D-UIO-66/PAN/PEO/LiTFSI CSE exhibited high ionic conductivity (2.89×10^{-4} S cm^{-1}), high Li^+ transference number (0.52), wide potential window (4.7 V), excellent interfacial compatibility, and outstanding ability to inhibit the growth of lithium dendrites. Consequently, the 3D-UIO-66/PAN/PEO/LiTFSI CSE is demonstrated to enable the stable cycling of a Li||Li symmetric cell, 20 μm thin Li||LFP cell, and high voltage Li||NMC cell. This work highlights the promising role of MOFs in realizing tunable ion transport as well as demonstrates the effectiveness and importance of constructing continuous ion transport pathways and 3D networks in SSEs, which provides a splendid strategy

on developing high-performance SSEs for high-energy and high safety batteries.

Declaration of Competing Interest

The authors declare that they have no known competing financial interests or personal relationships that could have appeared to influence the work reported in this paper.

Data Availability

Data will be made available on request.

CRediT authorship contribution statement

Zhongliang Li: Methodology, Formal analysis, Investigation, Writing – original draft. **Shuxian Wang:** Investigation, Validation, Software. **Junkai Shi:** Validation, Software. **Yang Liu:** Methodology, Software. **Siyan Zheng:** Resources, Data curation. **Hanqin Zou:** Resources, Data curation. **Yilin Chen:** Data curation. **Wenxi Kuang:** Data curation. **Kui Ding:** Validation, Visualization. **Luyi Chen:** Validation, Visualization. **Ya-qian Lan:** Visualization, Writing – review & editing. **Yue-peng Cai:** Supervision, Writing – review & editing, Funding acquisition. **Qifeng Zheng:** Conceptualization, Supervision, Formal analysis, Writing – review & editing, Funding acquisition.

Acknowledgments

This work was supported by the National Natural Science Foundation of China (No. 22005108), Natural Science Foundation of Guangdong Province (Nos. 2019A1515011460, 2019B1515120027), International Science and Technology Cooperation Project of Guangdong Province (Nos. 2019A050510038, 2021A0505030063), Research and Development (R&D) Project in Key Areas of Guangdong Province (2020B0101030005).

Supplementary materials

Supplementary material associated with this article can be found, in the online version, at doi:10.1016/j.ensm.2022.02.014.

References

[1] M. Armand, J.M. Tarascon, Building better batteries, Nature 451 (2008) 652–657.
[2] J.M. Tarascon, M. Armand, Issues and challenges facing rechargeable lithium batteries, Nature 414 (2001) 359–367.
[3] A. Manthiram, Materials challenges and opportunities of lithium ion batteries, J. Phys. Chem. Lett. 2 (2011) 176–184.
[4] X. Zhang, Y. Yang, Z. Zhou, Towards practical lithium-metal anodes, Chem. Soc. Rev. 49 (2020) 3040–3071.
[5] J. Liu, Z. Bao, Y. Cui, E.J. Dufek, J.B. Goodenough, P. Khalifah, Q. Li, B.Y. Liaw, P. Liu, A. Manthiram, Y.S. Meng, V.R. Subramanian, M.F. Toney, V.V. Viswanathan, M.S. Whittingham, J. Xiao, W. Xu, J. Yang, X.Q. Yang, J.G. Zhang, Pathways for practical high-energy long-cycling lithium metal batteries, Nat. Energy 4 (2019) 180–186.
[6] D. Lin, Y. Liu, Y. Cui, Reviving the lithium metal anode for high-energy batteries, Nat. Nanotechnol. 12 (2017) 194.
[7] Y. Jie, X. Ren, R. Cao, W. Cai, S. Jiao, Advanced liquid electrolytes for rechargeable Li metal batteries, Adv. Funct. Mater. 30 (2020) 1910777.
[8] C. Fang, X. Wang, Y.S. Meng, Key issues hindering a practical lithium-metal anode, Trends Chem. 1 (2019) 152–158.
[9] X.B. Cheng, R. Zhang, C.Z. Zhao, Q. Zhang, Toward safe lithium metal anode in rechargeable batteries: a review, Chem. Rev. 117 (2017) 10403–10473.
[10] S. Xia, X. Wu, Z. Zhang, Y. Cui, W. Liu, Practical challenges and future perspectives of all-solid-state lithium-metal batteries, Chem 5 (2019) 753–785.
[11] D. Zhou, D. Shanmukaraj, A. Tkacheva, M. Armand, G. Wang, Polymer electrolytes for lithium-based batteries: advances and prospects, Chem 5 (2019) 2326–2352.
[12] J.C. Bachman, S. Muy, A. Grimaud, H.H. Chang, N. Pour, S.F. Lux, O. Paschos, F. Maglia, S. Lupart, P. Lamp, L. Giordano, Y. Shao-Horn, Inorganic solid-state electrolytes for lithium batteries: mechanisms and properties governing ion conduction, Chem. Rev. 116 (2016) 140–162.
[13] Y. Zheng, Y. Yao, J. Ou, M. Li, D. Luo, H. Dou, Z. Li, K. Amine, A. Yu, Z. Chen, A review of composite solid-state electrolytes for lithium batteries: fundamentals, key materials and advanced structures, Chem. Soc. Rev. 49 (2020) 8790–8839.
[14] J. Wan, J. Xie, D.G. Mackanic, W. Burke, Z. Bao, Y. Cui, Status, promises, and challenges of nanocomposite solid-state electrolytes for safe and high performance lithium batteries, Mater. Today Nano 4 (2018) 1–16.
[15] Y. Kato, S. Hori, T. Saito, K. Suzuki, M. Hirayama, A. Mitsui, M. Yonemura, H. Iba, R. Kanno, High-power all-solid-state batteries using sulfide superionic conductors, Nat. Energy 1 (2016) 16030.
[16] H. Wang, L. Sheng, G. Yasin, L. Wang, H. Xu, X. He, Reviewing the current status and development of polymer electrolytes for solid-state lithium batteries, Energy Storage Mater. 33 (2020) 188–215.
[17] J. Lopez, D.G. Mackanic, Y. Cui, Z. Bao, Designing polymers for advanced battery chemistries, Nat. Rev. Mater. 4 (2019) 312–330.
[18] L. Chen, Y. Li, S.P. Li, L.Z. Fan, C.W. Nan, J.B. Goodenough, PEO/garnet composite electrolytes for solid-state lithium batteries: from "ceramic-in-polymer" to "polymer-in-ceramic, Nano Energy 46 (2018) 176–184.
[19] W. Liu, S.W. Lee, D. Lin, F. Shi, S. Wang, A.D. Sendek, Y. Cui, Enhancing ionic conductivity in composite polymer electrolytes with well-aligned ceramic nanowires, Nat. Energy 2 (2017) 17035.
[20] O. Sheng, C. Jin, X. Ding, T. Liu, Y. Wan, Y. Liu, J. Nai, Y. Wang, C. Liu, X. Tao, A decade of progress on solid-state electrolytes for secondary batteries: advances and contributions, Adv. Funct. Mater. 31 (2021) 2100891.
[21] C.Z. Zhao, X.Q. Zhang, X.B. Cheng, R. Zhang, R. Xu, P.Y. Chen, H.J. Peng, J.Q. Huang, Q. Zhang, An anion-immobilized composite electrolyte for dendrite-free lithium metal anodes, Proc. Natl. Acad. Sci. 114 (2017) 11069–11074.
[22] D. Li, L. Chen, T. Wang, L.Z. Fan, 3D fiber-network-reinforced bicontinuous composite solid electrolyte for dendrite-free lithium metal batteries, ACS Appl. Mater. Interfaces 10 (2018) 7069–7078.
[23] K.K. Fu, Y. Gong, J. Dai, A. Gong, X. Han, Y. Yao, C. Wang, Y. Wang, Y. Chen, C. Yan, Y. Li, E.D. Wachsman, L. Hu, Flexible, solid-state, ion-conducting membrane with 3D garnet nanofiber networks for lithium batteries, Proc. Natl. Acad. Sci. U. S. A. 113 (2016) 7094 -7049.
[24] J. Sun, X. Yao, Y. Li, Q. Zhang, C. Hou, Q. Shi, H. Wang, Facilitating interfacial stability via bilayer heterostructure solid electrolyte toward high-energy, safe and adaptable lithium batteries, Adv. Energy Mater. 10 (2020) 2000709.
[25] W. Liu, N. Liu, J. Sun, P.C. Hsu, Y. Li, H.W. Lee, Y. Cui, Ionic conductivity enhancement of polymer electrolytes with ceramic nanowire fillers, Nano Lett. 15 (2015) 2740–2745.
[26] H. Zhai, P. Xu, M. Ning, Q. Cheng, J. Mandal, Y. Yang, A flexible solid composite electrolyte with vertically aligned and connected ion-conducting nanoparticles for lithium batteries, Nano Lett. 17 (2017) 3182–3187.
[27] J. Wan, J. Xie, X. Kong, Z. Liu, K. Liu, F. Shi, A. Pei, H. Chen, W. Chen, J. Chen, X. Zhang, L. Zong, J. Wang, L.Q. Chen, J. Qin, Y. Cui, Ultrathin, flexible, solid polymer composite electrolyte enabled with aligned nanoporous host for lithium batteries, Nat. Nanotechnol. 14 (2019) 705–711.
[28] C.Z. Zhao, P.Y. Chen, R. Zhang, X. Chen, B.Q. Li, X.Q. Zhang, X.B. Cheng, Q. Zhang, An ion redistributor for dendrite-free lithium metal anodes, Sci. Adv. 4 (2018) eaat3446.
[29] L. Shen, H.B. Wu, F. Liu, J.L. Brosmer, G. Shen, X. Wang, J.I. Zink, Q. Xiao, M. Cai, G. Wang, Y. Lu, B. Dunn, Creating lithium-ion electrolytes with biomimetic ionic channels in metal-organic frameworks, Adv. Mater. 30 (2018) e1707476.
[30] H. Huo, B. Wu, T. Zhang, X. Zheng, L. Ge, T. Xu, X. Guo, X. Sun, Anion-immobilized polymer electrolyte achieved by cationic metal-organic framework filler for dendrite-free solid-state batteries, Energy Storage Mater. 18 (2019) 59–67.
[31] W. Xu, X. Pei, C.S. Diercks, H. Lyu, Z. Ji, O.M. Yaghi, A metal-organic framework of organic vertices and polyoxometalate linkers as a solid-state electrolyte, J. Am. Chem. Soc. 141 (2019) 17522–17526.
[32] F. Zhu, H. Bao, X. Wu, Y. Tao, C. Qin, Z. Su, Z. Kang, High-performance metal-organic framework-based single ion conducting solid-state electrolytes for low-temperature lithium metal batteries, ACS Appl. Mater. Interfaces 11 (2019) 43206–43213.
[33] Q. Zhang, B. Liu, J. Wang, Q. Li, D. Li, S. Guo, Y. Xiao, Q. Zeng, W. He, M. Zheng, Y. Ma, S. Huang, The optimized interfacial compatibility of metal–organic frameworks enables a high-performance quasi-solid metal battery, ACS Energy Lett. 5 (2020) 2919–2926.
[34] S.Y. Bai, Y. Sun, J. Yi, Y.B. He, Y. Qiao, H.S. Zhou, High-power Li-metal anode enabled by metal-organic framework modified electrolyte, Joule 2 (2018) 2117–2132.
[35] R. Zhao, Y. Wu, Z. Liang, L. Gao, W. Xia, Y. Zhao, R. Zou, Metal–organic frameworks for solid-state electrolytes, Energy Environ. Sci. 13 (2020) 2386–2403.
[36] J.H. Ahn, G.X. Wang, H.K. Liu, S.X. Dou, Nanoparticle-dispersed PEO polymer electrolytes for Li batteries, J. Power Sources 119-121 (2003) 422–426.
[37] R. Xu, Y. Xiao, R. Zhang, X.B. Cheng, C.Z. Zhao, X.Q. Zhang, C. Yan, Q. Zhang, J.Q. Huang, Dual-phase single-ion pathway interfaces for robust lithium metal in working batteries, Adv. Mater. 31 (2019) e1808392.
[38] Y. Yamada, J. Wang, S. Ko, E. Watanabe, A. Yamada, Advances and issues in developing salt-concentrated battery electrolytes, Nat. Energy 4 (2019) 269–280.
[39] X. Fan, L. Chen, X. Ji, T. Deng, S. Hou, J. Chen, J. Zheng, F. Wang, J. Jiang, K. Xu, C. Wang, Highly fluorinated interphases enable high-voltage Li-metal batteries, Chem 4 (2018) 174–185.
[40] O. Sheng, J. Zheng, Z. Ju, C. Jin, Y. Wang, M. Chen, J. Nai, T. Liu, W. Zhang, Y. Liu, X. Tao, *In situ* construction of a LiF-enriched interface for stable all-solid-state batteries and its origin revealed by cryo-TEM, Adv. Mater. 32 (2020) 2000223.
[41] Q. Zeng, J. Wang, X. Li, Y. Ouyang, W. He, D. Li, S. Guo, Y. Xiao, H. Deng, W. Gong, Q. Zhang, S. Huang, Cross-linked chains of metal–organic framework afford continuous ion transport in solid batteries, ACS Energy Lett. 6 (2021) 2434–2441.
[42] M. Yao, T. Yu, Q. Ruan, Q. Chen, H. Zhang, S. Zhang, High-voltage and wide-temperature lithium metal batteries enabled by ultrathin MOF-derived solid polymer electrolytes with modulated ion transport, ACS Appl. Mater. Interfaces 13 (2021) 47163–47173.